Up/Down and P/S Decompositions of Elastic Wavefields Using Complex Seismic Traces with Applications to Calculating Poynting Vectors and Angle-Domain Common-Image Gathers from Reverse Time Migrations

Citation:

Wang, W., G. A. McMechan, C. Tang, and F. Xie. 2015. "Up/down and P/S decompositions of elastic wavefields using complex seismic traces with applications to calculating Poynting vectors and angle-domain common-image gathers from reverse time migrations." Geophysics 81(4): S181-S194.

GEOPHYSICS, VOL. 81, NO. 4 (JULY-AUGUST 2016); P. S181–S194, 13 FIGS.
10.1190/GEO2015-0456.1

Up/down and P/S decompositions of elastic wavefields using complex seismic traces with applications to calculating Poynting vectors and angle-domain common-image gathers from reverse time migrations

Wenlong Wang[1], George A. McMechan[1], Chen Tang[1], and Fei Xie[2]

ABSTRACT

Separations of up- and down-going as well as of P- and S-waves are often a part of processing of multicomponent recorded data and propagating wavefields. Most previous methods for separating up/down propagating wavefields are expensive because of the requirement to save time steps to perform Fourier transforms over time. An alternate approach for separation of up-and down-going waves, based on extrapolation of complex data traces is extended from acoustic to elastic, and combined with P- and S-wave decomposition by decoupled propagation. This preserves all the information in the original data and eliminates the need for a Fourier transform over time, thereby significantly reducing the storage cost and improving computational efficiency. Wavefield decomposition is applied to synthetic elastic VSP data and propagating wavefield snapshots. Poynting vectors obtained from the particle velocity and stress fields after P/S and up/down decompositions are much more accurate than those without because interference between the corresponding wavefronts is significantly reduced. Elastic reverse time migration with the P/S and up/down decompositions indicated significant improvement compared with those without decompositions, when applied to elastic data from a portion of the Marmousi2 model.

INTRODUCTION

Multicomponent seismic data contain more information about the subsurface than single-component data, but it is also more difficult to process because both P/S wave modes coexist, and waves with different propagation directions may interfere. Wavefield decomposition improves understanding and analysis of elastic multicomponent wavefields. Wavefield decomposition can be based on propagation direction (e.g., up/down separation), which can be applied to acoustic and elastic wavefields, as well as P/S wave mode decomposition of elastic wavefields. The up/down and P/S decompositions can be in seismograms, which are recorded traces as a function of time, or in space-domain wavefield snapshots, at fixed times.

Up/down separation

Up- and down-going wave separation in seismograms is widely used in processing ocean-bottom seismometer (OBS) data and vertical seismic profile (VSP) data. Because of the differences in acquisition geometry, the up/down separation algorithms for OBS and VSP data are different. OBS data are usually contaminated by water-layer multiple reverberations (Weglein, 1999), but they can be separated into up-going (primaries) and down-going waves (multiples) by combining the pressure and the vertical geophone particle velocity components (White, 1965). The separated multiples can also be used in imaging of OBS data (Dash et al., 2009). VSP data recorders are distributed vertically in a borehole and thus can separate data into up-going and down-going parts in the τ-p domain (Hu and McMechan, 1987) or the ω-k domain (Wenschel, 1976; Hu and McMechan, 1987). Up/down separation of propagating wavefields also has significant value in removing low-frequency noise during reverse time migration (RTM) (Liu et al., 2011), and also for separating the contribution of forward and backward scattering when computing the velocity (modulus) gradients during full-waveform inversion (Tang et al., 2013b; Wang et al., 2013).

In Liu et al.'s (2011) method, up/down separation is implicit in a decomposed crosscorrelation image condition, and thus the sepa-

Manuscript received by the Editor 30 August 2015; revised manuscript received 1 March 2016; published online 23 May 2016.
[1]The University of Texas at Dallas (UT-Dallas), Center for Lithospheric Studies, Richardson, Texas, USA. E-mail: wxw120130@utdallas.edu; mcmec@utdallas.edu; chen.tang.diary@gmail.com.
[2]Exploration and Production Research Institute, Sinopec, Haidian, Beijing, China. E-mail: xiefei007007@126.com.

rated up- and down-going wavefields are not available, which limits its applications. Poynting vectors are also used to separate the wavefields according to propagation directions (Chen and He, 2014), and are not confined to the imaging process. Poynting vectors may give inaccurate propagation directions when two or more wavefronts interfere. Local plane-wave decomposition can also be used for up/down wavefield separation and for estimating propagation angles (Xie and Wu, 2002; Tang et al., 2013a). Plane-wave decomposition is usually performed in the frequency-wavenumber domain, which needs 4D spatiotemporal Fourier transforms of source and receiver wavefields, which is very expensive.

An alternative approach for determining propagation directions (and hence separating up-going and down-going waves), based on one-way propagation of complex traces is described by Zhang et al. (2007b) for acoustic waves, and applied by Tang and McMechan (2016) to calculate multidirection slowness vectors. A related application, based on Havlicek et al. (1998) shown by Zhang and McMechan (2011) uses Hilbert transforms to calculate instantaneous wavenumbers in x-z space to define reflector normals; another application by Jin et al. (2014), calculates wave propagation directions from phase gradients. The complex trace approach is the one we use below.

P/S plus up/down decompositions

All of the above studies use only acoustic data. The main new result of this paper is the extension to elastic wave propagation. For data from elastic media, besides the up/down separation, it is essential to decompose P- and S-waves as parts of seismic data processing, such as RTM, angle-domain common-image gather (ADCIG) extraction, and migration velocity analysis. P/S separation can be realized by using divergence and curl operators (Sun, 1999; Sun and McMechan, 2001) for isotropic media, or divergence-like and curl-like operators (Yan and Sava, 2008a) for anisotropic media. However, those operators alter the phase and amplitude of the original wavefield. On the other hand, P/S vector decomposition (Zhang and McMechan, 2010), which preserves all the components of P- and S-waves, has shown its superiority in terms of accuracy of the phase and amplitude in the context of data for isotropic elastic media (Wang et al., 2015). P/S vector decomposition algorithms are available for isotropic (Ma and Zhu, 2003; Zhang et al., 2007a; Xiao and Leaney, 2010; Wang et al., 2015) and anisotropic (Zhang and McMechan, 2010) media. In this paper, we combine the P/S and up/down decompositions.

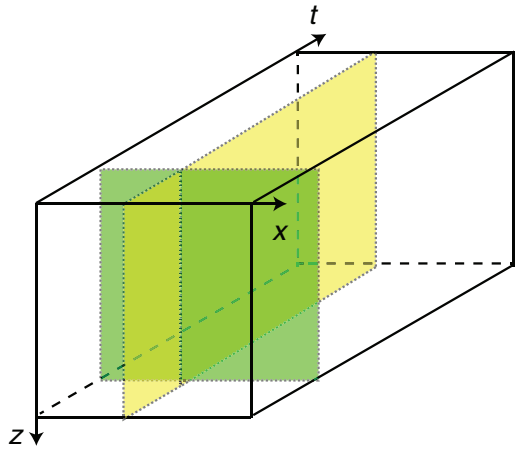

Figure 1. Acoustic or elastic wavefields represented as slices through a t-x-z volume. VSP data are represented with a t-z slice (yellow) at a constant x of the volume; an x-z wavefield snapshot (green) is an x-z slice at a constant t.

In the following sections, we first illustrate the methodology of up/down wavefield separation using complex traces for multicomponent data, and then combine it with P- and S-wave decomposition during elastic wave propagation. Examples include up/down separation of elastic VSP data and propagating wavefield snapshots, decomposition of Poynting vectors of multiple overlapping up- and down-going P- and S-waves. Finally, elastic RTMs are performed on a part of Marmousi2 model to generate PP and PS ADCIGs based on P/S and up/down wavefield decompositions and decomposed Poynting vectors. A comparison is made with the RTM results without decompositions and with only P/S decomposition. All the examples are in 2D, but the algorithm can be extended to 3D.

METHODOLOGY

Previous up/down separations (ω-k domain separation)

Up/down separation algorithms for elastic wavefields are similar to those for acoustic data, and are mostly based on the sign of the apparent propagation velocity v_z, or slowness p_z ($= v_z^{-1}$) along the depth z-axis. Thus, the input is the (t, z) slice (a VSP) at any x of a t-x-z volume, or a series of (fixed-time) snapshots on a 2D (x, z) space plane (Figure 1). For acoustic and elastic wavefields, v_z can be calculated using the dispersion relation produced by the 2D Fourier transform, of the input t-z slice, to ω-k_z, which gives

$$v_z = \omega/k_z, \tag{1}$$

or, in term of the apparent vertical slowness

$$p_z = k_z/\omega, \tag{2}$$

where ω is the angular frequency and k_z is the apparent vertical wavenumber. A straightforward way to separate up- and down-going waves in VSP data (a t-z slice at fixed x), or in a wavefield snapshot (an x-z slice at fixed t) is via the 2D Fourier transform, of the t-z slice at each fixed x of the t-x-z volume, into ω-k_z (Hu and McMechan, 1987) and using the criteria

$$\mathbf{S}_D(\omega, k_z) = \begin{cases} \mathbf{S}(\omega, k_z), & \text{if } \omega/k_z \geq 0, \\ 0, & \text{if } \omega/k_z < 0, \end{cases} \tag{3}$$

and

$$\mathbf{S}_U(\omega, k_z) = \begin{cases} \mathbf{S}(\omega, k_z), & \text{if } \omega/k_z < 0, \\ 0, & \text{if } \omega/k_z \geq 0, \end{cases} \tag{4}$$

where $\mathbf{S}(\omega, k_z)$ is the 2D Fourier transform of the acoustic, or a component of the elastic, wavefield (spatial dimensions other than z are omitted for simplicity). $\mathbf{S}_U$ and $\mathbf{S}_D$ are the separated up- and down-going wavefields, respectively, in the ω-k_z domain, which are then transformed back to t-z. This procedure needs to be applied to each component individually of the elastic wavefield for up/down separation.

This method is applicable for separating the acoustic and elastic VSP data, where the time sequences are in the 2D (t-z) recorded data. However, for separation of the propagating wavefield snapshots in x-z, this becomes expensive because the time sequence must be complete to perform the 2D Fourier transforms over time, which means that a 3D (t-x-z) volume needs to be stored for time-domain extrapolations, thus making it costly. This can be simplified, with no loss of accuracy, and with a significant reduction in cost, by using complex traces.

Up/down separation using complex traces

Equations 3 and 4 require knowing ω before up/down separation, but calculating ω involves a temporal Fourier transform, which is expensive. However, note that only the sign of ω is needed for the separation criteria in equations 3 and 4; thus, if the sign of ω can be set to be "+" without changing the wavefield, then, the temporal Fourier transform is no longer needed, and the process of separation into down-going waves $\mathbf{S}_D$ and up-going waves $\mathbf{S}_U$ can be performed in the t-k_z domain using

$$\mathbf{S}_D(t,k_z)=\begin{cases}\mathbf{S}(t,k_z), & \text{if } k_z\geq 0,\\ 0, & \text{if } k_z<0,\end{cases} \tag{5}$$

and

$$\mathbf{S}_U(t,k_z)=\begin{cases}\mathbf{S}(t,k_z), & \text{if } k_z<0,\\ 0, & \text{if } k_z\geq 0,\end{cases} \tag{6}$$

which are more efficient than equations 3 and 4 because they require only a 1D Fourier transform over the z-axis, which is present in the VSP data and in x-z wavefield snapshots (Zhang et al., 2007b; Tang and McMechan, 2016); thus, once the sign of ω is fixed, the up/down separation can be easily performed at any desired time step.

Seismic waves are real-valued signals, whose Fourier transforms (spectra) are complex and conjugate symmetric; the negative frequency half of the spectrum is the conjugate of the positive frequency half (Maple, 1999). Gabor (1946) and Ville (1948) create the so-called analytic signal in signal processing to remove this spectral redundancy. The analytic signal is also called the complex trace $\tilde{\mathbf{d}}$ in seismology, and it can be constructed using the original real-valued seismic trace d as the real part, and the Hilbert transform $\mathcal{H}$ of the original trace as the imaginary part

$$\tilde{\mathbf{d}}=\mathbf{d}+i\mathcal{H}[\mathbf{d}]. \tag{7}$$

The Hilbert transform can be calculated via Fourier transforms, but special attention needs to be given to the zero and Nyquist frequencies; see Appendix A for a specific procedure for numerical generation of discrete-time analytic signals.

To illustrate the properties of complex traces, consider a Ricker wavelet with dominant frequency of 15 Hz and 0.5 ms time interval as the input (Figure 2a); this is a real signal that has a symmetric amplitude spectrum in the frequency domain (the solid blue line in Figure 2b). Figure 2c and 2d shows the Hilbert transform of Figure 2a and the corresponding frequency-domain spectrum. Note, the amplitude spectrum (the blue line) of Figure 2d is the same as that in Figure 2b, but the phase (dashed green line) is shifted by 90°. We use Figure 2a as the real part and Figure 2c as the imaginary part to construct the complex trace Figure 2e, after a complex Fast Fourier Transform (FFT), the amplitude spectrum and wrapped phase are shown in Figure 2f; note that the amplitude spectrum at negative frequencies is zero, and the positive frequency half is scaled by two; the wrapped phase is the same as that of original input data (Figure 2b).

The complex trace (Figure 2e) contains the same information (in its phase and scaled amplitude) as the input wave, and more importantly, the negative frequency part is always zero (Figure 2f) for any real signal as input, which makes the up/down wavefield separation scheme with equations 5 and 6 applicable. The result is that the original real-valued signal (Figure 2a) has now become complex-valued (Figure 2e). In the next subsection, we show specific examples of using complex traces to separate up- and down-going waves in elastic (t-z) VSP data and wavefield (x-z) snapshots.

Algorithm implementations and applications

Up/down and P/S decompositions of elastic (t-z) VSP data

The VSP data are obtained by excitation of a source on the surface, with traces recorded in a borehole, as functions of depth z and time t. Elastic VSP data $\mathbf{d}(t,z)$ have more than one component, and each component of the original VSP signal $\mathbf{d}(t,z)$ can be processed to a complex signal $\tilde{\mathbf{d}}(t,z)$ for each recording depth using equa-

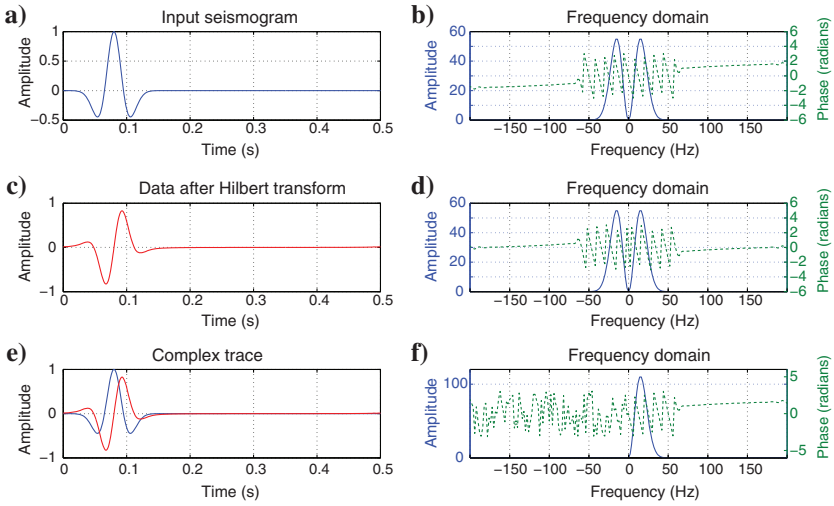

Figure 2. (a) The input seismic trace (a Ricker wavelet) in the time domain; (b) the Fourier transform of panel (a); (c) the Hilbert transform of panel (a), notice that panels (b and d) have the same symmetric amplitude spectra; only the phases are shifted by 90°. (e) The complex trace constructed using equation 7 with the panel (a) (blue) as real part and panel (c) (red) as imaginary part and (f) the complex trace spectrum. The solid blue and dashed green curves in panels (b, d, and f) are the amplitude spectra and wrapped phases, respectively. (e) The complex trace has a nonzero amplitude spectrum only for (f) positive frequencies, and its amplitude is doubled compared with panels (b and d). The zero-frequency point is shifted to the middle of the spectra in Figure 2b, 2d, and 2f for easier visualization.

tion 7. Then, the up/down separation is achieved by forward FFTs over the z-axis to the t-k_z domain and applying the criteria in equations 5 and 6, followed by inverse FFTs back to the t-z domain. Each component of the VSP data is processed separately, which means the number of resultant pairs of separated up- and down-going waves is the same as the number of components in the original data (one pair for acoustic data, two pairs for 2C elastic data, and three pairs for 3C elastic data). The amplitude and phase of the input data are preserved in the separated up-going and down-going VSP data. This VSP separation scheme is equivalent to ω-k_z domain separation (Hu and McMechan, 1987).

The P- and S-waves coexist in an elastic VSP, and are not decomposed using only this process. A viable P- and S-wave decomposition for surface (t-x) gather data is proposed by Sun (1999) and Sun and McMechan (2001). In Sun's algorithm, the wavefield recorded at the surface is extrapolated downward into a velocity model to an arbitrary reference datum, then it is separated into scalar P- and S-waves by divergence and curl calculations, which are then individually extrapolated upward to reconstruct the separate P- and S-waves at their originally recorded positions; this requires amplitude and phase correction as part of the divergence and curl operations. Here, following Wang et al. (2015), we use a similar process, but used decoupled propagation instead of curl and divergence (so corrections are not needed). This can also be applied to elastic (t-z) VSP data. The procedure uses the recorded VSP data as boundary conditions to first perform a reverse time, leftward (or rightward, depending on the 2D geometry of the source and receiver positions) reconstruction of the propagating elastic wavefield using decoupled propagation (Ma and Zhu, 2003; Xiao and Leaney, 2010; Wang et al., 2015). The reconstructed decomposed P-wave is saved at a vertical line of virtual receivers, which is located near the real line of VSP receivers. Then, a forward-time, rightward (or leftward) extrapolation is performed, with the reconstructed P-wave data, from the virtual receivers. This reconstructed P wavefield is recorded again at the same times and positions as the real VSP receivers, to give the decomposed P-wave VSP data. Finally, a subtraction of the reconstructed P-wave data from each component of the original VSP yields the decomposed S-wave VSP data (see figure 5 of Wang et al. [2015] for a particle velocity example, and see Appendix B below for a derivation for the stresses).

To illustrate the separation of elastic VSP data, we design a 256 × 256 two-layer model (Figure 3) with grid increment $h = 5$ m. The

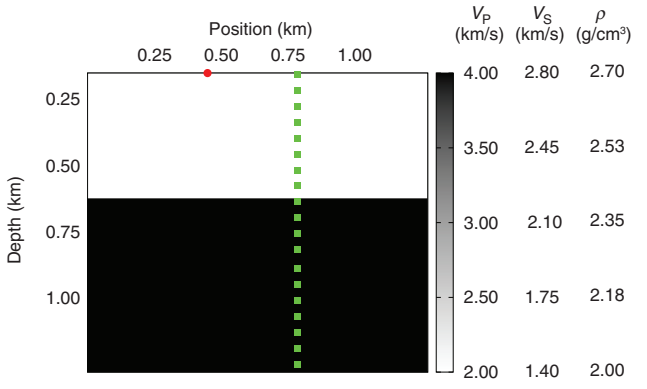

Figure 3. Two-layer P-wave velocity V_P, S-wave velocity V_S, and density ρ model for generating elastic VSP data (Figure 4a and 4b). The red spot is the source location; the green squares are every 14th receiver in a borehole.

source is placed at $(x, z) = (0.45, 0.00)$ km, and the receivers are placed in a borehole at $x = 0.80$ km with vertical spacing 5 m from (0.80, 0.00) to (0.80, 1.28) km (the green squares in Figure 3). The time increment for recording is 0.5 ms. A 2D staggered-grid finite-difference formulation is used for solving the elastodynamic (Virieux, 1986; Levander, 1988) equations, with eighth-order accuracy in space and second-order accuracy in time. Convolutional perfectly matched layer (CPML) absorbing boundary conditions (Komatitsch and Martin, 2007) with a width of 20 grid points outside the models are applied on all four grid edges to reduce unwanted edge reflections during wave propagation. This extrapolator is used in all the following elastic synthetic tests in this and the next section. The CPML boundary zones are not included in the plotted snapshots or images.

The observed elastic (particle velocity) VSP data (Figure 4a for horizontal and Figure 4b for vertical components) contain up-going and down-going P- and S-waves. As the source for the VSP is offset, all receivers will record nonzero amplitudes on both components. We first decompose the elastic VSP into P (Figure 4c and 4d) and S (Figure 4e and 4f) parts (see the procedure described in the previous section and in Wang et al., 2015), each with their horizontal and vertical components. Then, we apply the up/down separation to each component of the decomposed P- and S-waves to obtain the down-going P-wave (Figure 4g and 4h), the down-going S-wave (Figure 4i and 4j), the up-going P-wave (Figure 4k and 4l), and the up-going S-wave (Figure 4m and 4n). The P/S decomposition of VSP data is achieved at the cost of two wavefield extrapolations, but when either the up/down separation or the P/S decomposition is not required, the other can be applied directly to the original VSP data because the processes of the up/down and P/S decompositions are independent.

Up/down and P/S decompositions of (x,z) elastic wavefield snapshots

Complex traces can also be used to separate up-going and down-going waves in fixed-time (x, z) snapshots during wavefield propagation. We use the complex traces as boundary conditions for the complex elastic wave equation

$$\rho \frac{\partial^2 \tilde{\mathbf{u}}}{\partial t^2} = (\lambda + 2\mu)\nabla(\nabla \cdot \tilde{\mathbf{u}}) - \mu \nabla \times \nabla \times \tilde{\mathbf{u}}, \qquad (8)$$

where λ and μ are the Lamé parameters and ρ is the density. Here, the extrapolated elastic wavefield $\tilde{\mathbf{u}}$ is the complex wavefield. The dot ($\cdot$) denotes a dot product and the cross ($\times$) denotes a cross product.

Because the isotropic elastic wave equation 8 is a linear partial differential equation, and all other parameters (λ, μ, and ρ) are real numbers, the complex wave equations can either be solved directly using complex wavefield extrapolation or decomposed into two real parts, each of which can be extrapolated separately and independently using the real and imaginary parts of the complex traces. The first term on the right side of equation 8 propagates only P-waves, and the second term propagates only S-waves; this is how decoupled elastic propagation works.

The specific procedures to perform the up/down separation of an (x, z) propagating wavefield are shown in the flowchart in Figure 5 and are described as follows:

1) Use equation 7 to generate a complex wavelet.
2) Extrapolate the complex wavefield from the complex source using the elastic extrapolator. Two approaches are available: (a) construct and extrapolate the complex wavefield directly by allocating complex arrays and using complex-number calculations for extrapolation, or (b) extrapolate two real wavefields using the real and imaginary parts of the complex seismograms, separately. Thus, for each time step, two wavefields are calculated; one corresponds to the real part and the other corresponds to the imaginary part of the complex wavefield. If the stress-velocity formulation (Virieux, 1986; Levander, 1988) is used for elastic extrapolation as we do here, the particle velocity and stress/pressure components are complex, and can be separated into up- and down-going parts.
3) At any desired time step, perform complex 1D Fourier transforms of each component of the extrapolated complex wavefield over the z-axis, to the k_z wavenumber domain, and do separate inverse Fourier transforms of the positive and negative wavenumbers back to the space domain. The wavefield of negative wavenumbers is the up-going wavefield; the wavefield of positive wavenumbers is the down-going wavefield.

The main new result in this paper is to combine elastic P- and S-wave vector decomposition and the up/down separation, and thus to further decompose an elastic wavefield into up-going P, up-going S, down-going P, and down-going S wavefields. Each decomposed wavefield also preserves all its components; and thus for all four decomposed wavefields, the phase and amplitudes are correct. The implementation is similar to the procedure discussed above; the decoupled propagation (Xiao and Leaney, 2010; Wang et al., 2015) is used in the complex wavefield extrapolation, so at each time step, we have both decomposed P/S complex wavefields, and the four (up-going and down-going P as well as up-going and down-going S) wavefields are obtained by performing step 3 on the P- and S-wavefields separately. The benefits of performing P/S plus up/down wavefield decompositions include decomposition of the Poynting vectors and application to elastic RTMs.

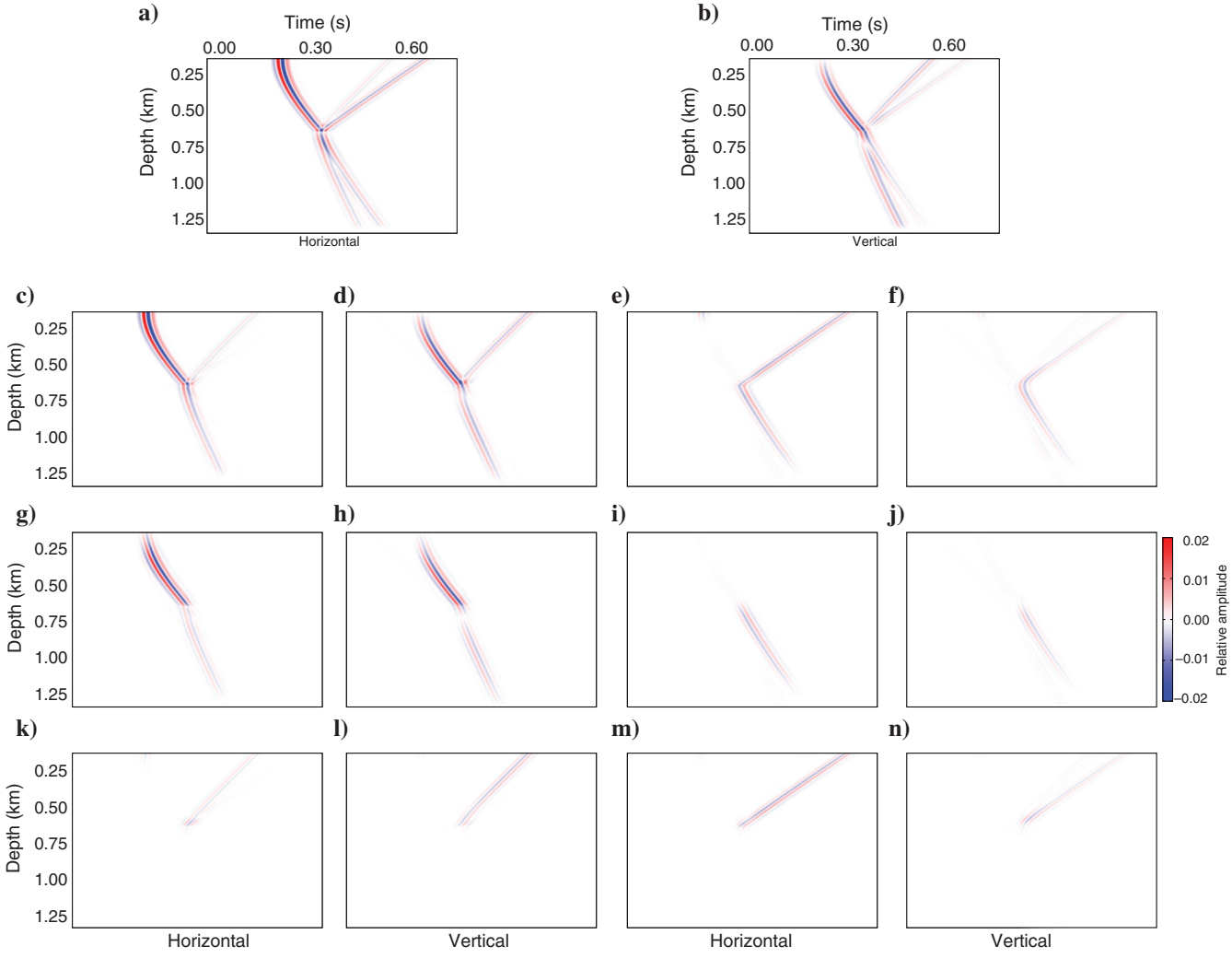

Figure 4. (a and b) Horizontal and vertical particle velocity components of the observed elastic VSP data; (c and d) the horizontal and vertical components of the decomposed P-wave; (e and f) the horizontal and vertical components of the decomposed S-wave; (g and h) the down-going P-wave; (i and j) the down-going S-wave; (k and l) the up-going P-wave; and (m and n) the up-going S-wave.

The up/down separation of a propagating elastic wavefield is performed on a 256×256 homogeneous isotropic elastic model (Figure 6a and 6b) with grid increment $h = 5$ m and time increment $dt = 0.5$ ms. The source is a composite (P/S) source, which generates P- and S-waves. A snapshot of the elastic wavefield is shown in Figure 6a and 6b for the horizontal and vertical components, respectively. Decoupled propagation (see Ma and Zhu, 2003; Zhang et al., 2007a; Xiao and Leaney, 2010; Chen, 2014; Wang and McMechan, 2015; Wang et al., 2015) is used to decompose the elastic wavefield into P- and S-waves, followed by the up/down separation. The P/S and up/down separations preserve the vector information of the input wavefield. The resultant decomposed P/S wavefields have horizontal and vertical components of the up- and down-going waves after separation (for a total of eight components; Figure 6).

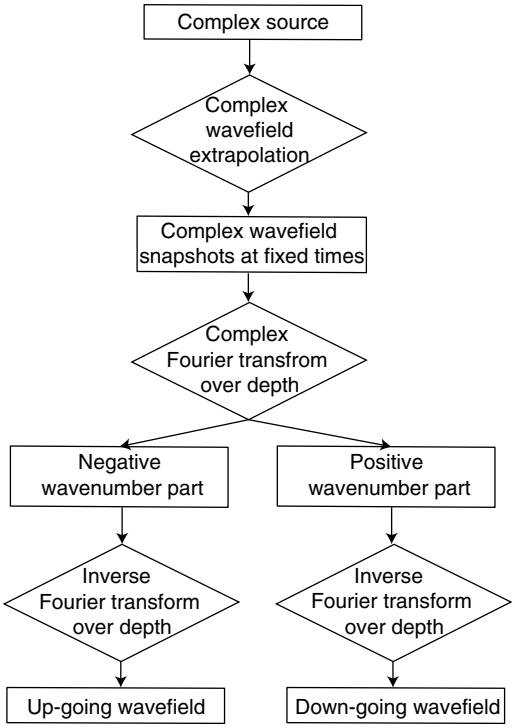

Figure 5. Flowchart of the procedures for the up/down wavefield separation. The input complex source or seismic traces can be generated using equation 7. For multicomponent elastic wavefields, the forward and inverse Fourier transforms are performed on each component.

POYNTING VECTOR DECOMPOSITION

An important application of the composite P/S decomposition and up/down wavefield separation is in calculating Poynting vectors. The Poynting vector shows flexibility and efficiency in calculating propagation directions for obtaining ADCIGs during RTM. However, a propagating wavefield usually contains superimposed waves propagating in different directions. Poynting vectors fail to give correct propagation directions where wavefronts overlap (including where the incident and reflected waves are coincident at a sharp velocity boundary in the migration velocity model) (Wang et al., 2016) because the Poynting vector gives only the overall energy flow direction (Červený, 2001). This problem can be substantially alleviated by up/down separation and P/S wavefield decomposition prior to calculating the Poynting vectors. The general particle velocity and stress form of a Poynting vector $\mathbf{s}$ is (Červený, 2001; Dickens and Winbow, 2011)

$$s_j = -\tau_{jk} v_k, \tag{9}$$

where j and k indicate the x- or z-component (in 2D), τ_{jk} is the stress tensor for an elastic wavefield; v_k is the kth component of the particle-velocity; and the repeated indices imply summation. Because we use the stress-particle-velocity formulation for extrapolation, vector components of stress and particle velocity are already

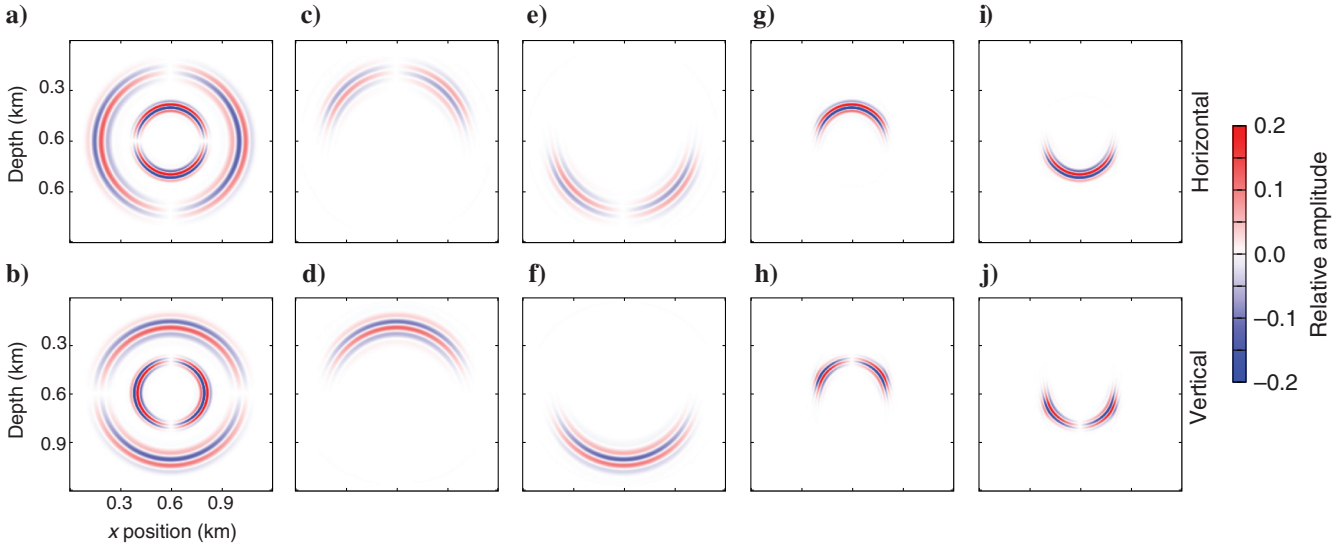

Figure 6. (a and b) Snapshots of the horizontal and vertical components of 2D elastic wave propagation in a homogeneous elastic medium with a composite (P/S) source at the center; (c and d) the components of the up-going P-waves; (e and f) the components of the down-going P-waves; (g and h) the components of the up-going S-waves; and (i and j) the components of the down-going S-waves.

available at each time step for calculating the Poynting vectors at each time step. An instability exists when using an amplitude or phase derivative method (not equation 9) to calculate propagation directions at peaks or troughs of a wavelet because the direction is undefined at these points; possible solutions include a time-lapse modification (Tang et al., 2013b) or optical flow (Yan and Ross, 2013; Zhang, 2014).

We use complex wavefield extrapolations to realize the up- and down-going wavefield separations; however, the variables in equation 9 need to be real valued, which means that the Poynting vectors have to be calculated after the up- and down-going wavefield separation. Thus, we first decompose the P- and S-waves, then separate these into up- and down-going parts, and finally we apply equation 9 for each of the four parts separately to obtain their corresponding Poynting vectors.

The decomposed P- and S-wave Poynting vectors can be calculated as (Wang and McMechan, 2015)

$$s_j^P = -\tau^P v_j^P, \tag{10}$$

for the P-wave, where v_j^P are the components of decomposed P-wave particle-velocity and τ^P is the P-wave stress. For the S-wave

$$S_j^S = -[\tau_{jk} - \tau^P \delta(j-k)] v_k^S, \tag{11}$$

where v_k^S is the kth component of the decomposed S-wave particle-velocity vector and δ is the Dirac delta function. The rationality of equations 10 and 11 is explained in Appendix B. All the Poynting vectors are calculated after the P/S and up/down decomposition algorithms are applied.

For illustration, consider a test with four intersecting wavefronts in a homogeneous medium: Two are explosive (P-waves), and two are rotational (S-waves). Horizontal and vertical components of particle velocity of an elastic, fixed-time snapshot are captured in Figure 7. The region of intersection of the four wavefronts (in the green boxes in Figure 7) is extracted, and Poynting vectors are calculated and superimposed as the black arrows in Figure 8a. The length of each arrow is the relative magnitude of the Poynting vector at the grid point at the tail of the arrow. The Poynting vectors are inaccurate where the wavefronts overlap, but after the P/S vector decomposition, followed by up/down separation, the wavefield and Poynting vectors are decomposed into four parts: the up-going P-wave (Figure 8b), the down-going P-wave (Figure 8c), the up-going S-wave (Figure 8d), and the down-going S-wave (Figure 8e), in which all the corresponding Poynting vectors are pointing in their correct propagation directions, normal to the wavefronts.

ELASTIC RTM WITH P/S AND UP/DOWN DECOMPOSITIONS

The up/down and P/S wavefield decompositions as well as the elastic Poynting vector computations are beneficial when used in elastic RTMs and for calculating PP/PS ADCIGs, as the source and receiver wavefields are then treated in a physically correct way. We can choose the desired decomposed wavefields to construct the images while avoiding crosstalk interference with other unwanted parts, which create artifacts. Below, we use a portion of a resampled Marmousi2 model (Martin et al., 2002) (the left column of Figure 9) to illustrate; the model is modified by substituting solid material with nonzero S-velocity for the uppermost water layer. The grid spacings in the x- and z-directions are 5 m. Two hundred sources are excited on the surface of the model from $x = 500$ to 4500 m with a horizontal spacing of 20 m. A fixed array of 1001 receivers is located along the model surface from $x = 0$ to 5000 m with 5 m spacing; all the receivers record data from all the sources. The time increment is 0.5 ms.

To illustrate the benefits of the decompositions, three elastic RTMs are performed independently using the same recorded data; the P-velocity, S-velocity, and density models are slightly smoothed (right column of Figure 9) to apply decoupled propagation (see Wang et al., 2015 for explanations). All the RTM images are constructed using a forward-time extrapolated source wavefield cross-correlated with a reverse time extrapolated receiver wavefield; the new key aspect is that the source and receiver wavefields are decomposed.

Elastic RTM and ADCIGs without wavefield decompositions

The first elastic RTM (Figure 10) is performed without up/down or P/S decompositions; the image is obtained by crosscorrelating corresponding elastic (x and z) components

$$\mathbf{I}_{xx}(x,\theta) = \int_0^{T_{\max}} \mathbf{S}_x(x)\mathbf{R}_x(x)dt, \tag{12}$$

and

$$\mathbf{I}_{zz}(x,\theta) = \int_0^{T_{\max}} \mathbf{S}_z(x)\mathbf{R}_z(x)dt, \tag{13}$$

where $\mathbf{S}$ and $\mathbf{R}$ are the source and receiver particle velocity wavefields, and the subscripts x and z denote the horizontal and vertical

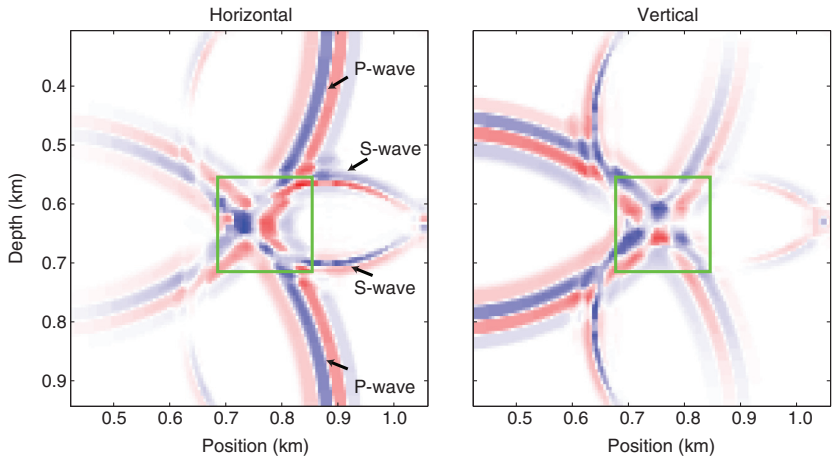

Figure 7. Snapshots of horizontal and vertical particle velocities of elastic waves from two explosive and two rotational sources. The magnified in part of the wavefront intersection part (in the green boxes) of the horizontal component with the extracted Poynting vectors, before and after P/S decomposition and up/down separation, are shown in Figure 8.

components, respectively; the time variable t in the wavefields is implicit, and thus it is omitted in these and the following equations. Crosscorrelation of components is commonly used for multicomponent elastic migrations (Yan and Sava, 2008b), but it is difficult to interpret physically. The angles θ for generating ADCIGs are calculated using the Poynting vectors of equation 9, which give only one incident angle for each image point at each image time; thus, the angles for $\mathbf{I}_{xx}$ and $\mathbf{I}_{zz}$ are the same. Figure 10 shows the stacked (Figure 10a) $\mathbf{I}_{zz}$ and (Figure 10b) $\mathbf{I}_{xx}$ images and corresponding representative ADCIGs. The $\mathbf{I}_{zz}$ and $\mathbf{I}_{xx}$ ADCIGs do not give flat events, which are expected when using the correct velocity models for migration, mainly because unseparated P- and S-waves are crosscorrelated to generate artifacts and the angles are not calculated correctly where different wavefronts overlap. The $\mathbf{I}_{xx}$ ADCIGs also suffer from inconsistent polarities at the same image points, which result in destructive stacking.

Elastic RTM and ADCIGs with P/S decomposition

The second elastic RTM (Figure 11) has only P/S decomposition applied, and we use the vector-based crosscorrelation imaging conditions (Wang and McMechan, 2015)

$$\mathbf{I}_{PP}(x,\theta) = \int_0^{T_{\max}} \mathrm{sgn}_{\mathrm{PP}}(x,\theta)\mathbf{S}_P(x)\mathbf{R}_P(x)dt, \qquad (14)$$

and

$$\mathbf{I}_{PS}(x,\theta) = \int_0^{T_{\max}} \mathrm{sgn}_{\mathrm{PS}}(x,\theta)\mathbf{S}_P(x)\mathbf{R}_S(x)dt, \qquad (15)$$

where the $\mathbf{S}$ and $\mathbf{R}$ are now the magnitudes of the source and receiver particle velocity wavefield vectors, with subscripts P and S for decomposed P- and S-waves, respectively. The $\mathrm{sgn}_{\mathrm{PP}}$ and $\mathrm{sgn}_{\mathrm{PS}}$ denote the sign of PP and PS reflections at the corresponding image point and image time, and are determined by the relative relations between the propagation and particle motion directions (for detailed explanations, see Wang and McMechan, 2015). The angles for PP and PS ADCIGs are calculated using the P/S decomposed Poynting vectors.

Figure 11 shows the stacked (Figure 11a) $\mathbf{I}_{PP}$ and (Figure 11b) $\mathbf{I}_{PS}$ images and the corresponding representative ADCIGs. Compared with Figure 10, the ADCIGs are much flatter and more coherent; the polarities of $\mathbf{I}_{PP}$ and $\mathbf{I}_{PS}$ are consistent over incident angles. The $\mathbf{I}_{PS}$ has higher resolution than $\mathbf{I}_{PP}$ because the wave-

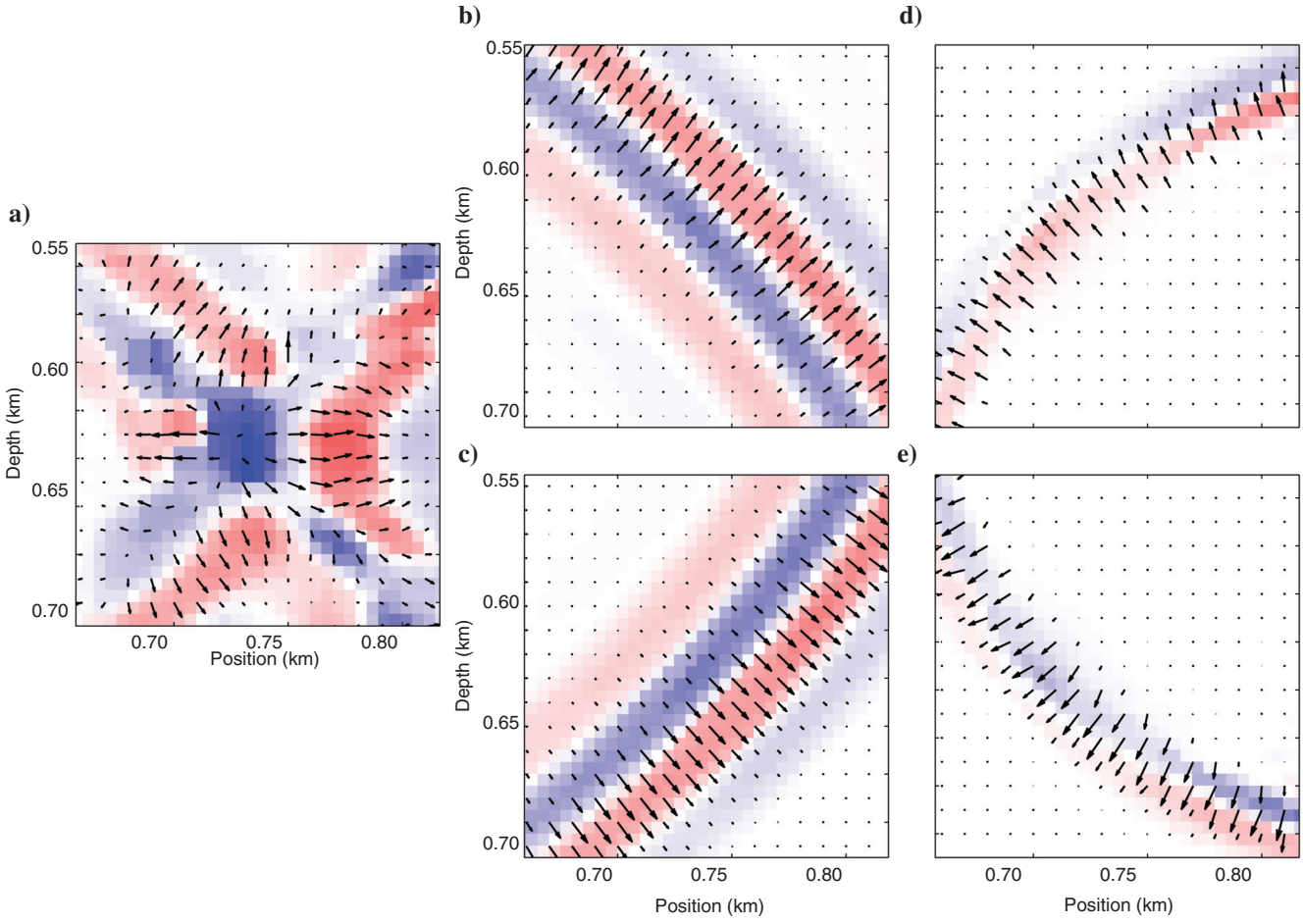

Figure 8. (a) Part of the horizontal component of the elastic wavefield (in color) from Figure 7, superimposed with Poynting vectors before wavefield separations. After the P/S vector decomposition, followed by up/down direction separation, the wavefields and their corresponding Poynting vectors are decomposed into: (b) the up-going P-wavefield, (c) the down-going P-wavefield, (d) the up-going S-wavefield, and (d) the down-going S-wavefield.

length of the S-wave is shorter than that of the P-wave. Also, the poor coherence of the $\mathbf{I}_{xx}$ ADCIGs caused by P-S crosstalk in Figure 10b is substantially reduced after the P/S decomposition in Figure 11b, and there is a corresponding improvement in the $\mathbf{I}_{PS}$ stack compared with the $\mathbf{I}_{xx}$ stack. The low-frequency high-amplitude artifacts observed in the $\mathbf{I}_{xx}$ (horizontal) component image in Figure 10b are now moved to the $\mathbf{I}_{PP}$ stacked image; from its ADCIGs, we see the artifacts come from the large angles, and are the result of subhorizontally propagating wide angle turning waves and backscatterings. A good solution to remove these artifacts is to apply the up/down separation.

Elastic RTM and ADCIGs with P/S and up/down decompositions

The third elastic RTM is performed with P/S and up/down decompositions. A total of 16 images may be generated by permutation of the crosscorrelated wave modes (P or S) and propagation directions (up or down); here, we show only the crosscorrelation results of down-going source P-waves $\mathbf{S}_P^d$ with up-going receiver P-waves $\mathbf{R}_P^u$ and S-waves $\mathbf{R}_S^u$

$$\mathbf{I}_{PP}^{du}(x,\theta) = \int_0^{T_{\max}} \mathrm{sgn}(x,\theta)\mathbf{S}_P^d(x)\mathbf{R}_P^u(x)dt, \qquad (16)$$

and

$$\mathbf{I}_{PS}^{du}(x,\theta) = \int_0^{T_{\max}} \mathrm{sgn}(x,\theta)\mathbf{S}_P^d(x)\mathbf{R}_S^u(x)dt, \qquad (17)$$

where the superscripts u and d denote the up- and down-going waves. Figure 12 shows the stacked (Figure 12a) $\mathbf{I}_{PP}^{du}$ and (Figure 12b) $\mathbf{I}_{PS}^{du}$ images and corresponding representative ADCIGs. Generating other decomposed images (e.g., $\mathbf{I}_{PP}^{ud}$ and $\mathbf{I}_{PS}^{ud}$) follow the same format of equations 16 and 17, which shows the flexibility of the proposed algorithm. However, Fei et al. (2014) observe artifacts

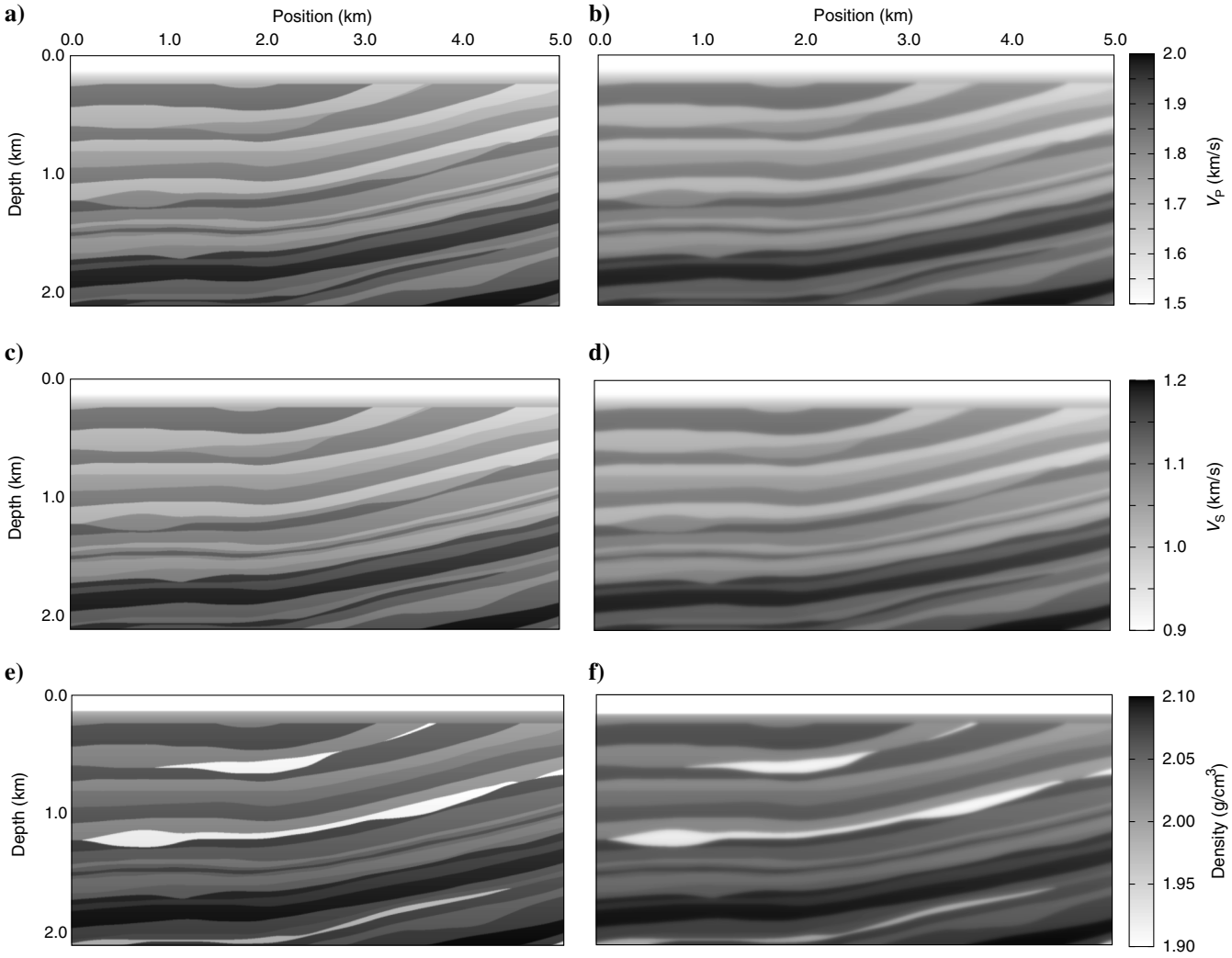

Figure 9. (a) P-wave velocity, (c) S-wave velocity, and (e) density distributions used for isotropic elastic wavefield modeling; (b, d, and f) smoothed models of panels (a, c, and e), respectively. This is a portion of the Marmousi2 model.

in $\mathbf{I}^{du}$ from acoustic RTMs; thus, the elastic $\mathbf{I}^{du}$ images are not illustrated here (for additional discussions, see Wang et al., 2016).

Figures 11 and 12 give clear and correct structures of the model. The overall magnitudes in the stacks in Figure 12 are smaller than those in Figure 11 because only a portion of the P/S waves are retained after the up/down separation. The low-frequency high-amplitude artifacts are much reduced in Figure 12a because only wavefields with opposite propagation directions along the depth axis are crosscorrelated; thus, imaging of turning waves and backscatterings is avoided. The stacked PS images in Figures 11b and 12b show much wider illumination than the $\mathbf{I}_{xx}$ in Figure 10b. The artifacts, which are strong at depths less than 1 km, are progressively reduced (from Figure 10) by applying the P/S decomposition (Figure 11) and then the up/down separation (Figure 12). There are two additional features of interest that are produced automatically in the representative PS ADCIGs in Figure 12b; these are that the converted wave amplitudes are correctly recovered as zero at 0° incident angle, and that the PS reflection polarities are the same to either side of 0°. Thus, no polarity correction is needed prior to stacking to obtain the $\mathbf{I}_{PS}$ image of the left panel of Figure 12b. These are clear advantages of the proposed algorithm.

Another popular way to remove the low-frequency artifacts is to apply Laplacian filters. Figure 13a and 13b shows the Laplacian filtered PP and PS images using the stacked images in Figure 11a and 11b as input. The low-frequency artifacts in Figure 11a are removed, but the phase and amplitude of the filtered images (Figure 13a and 13b) are changed compared with the input images (Zhang and Sun, 2009). On the other hand, the amplitudes and the phases of images in Figure 12 are scaled the same as those in Figure 11.

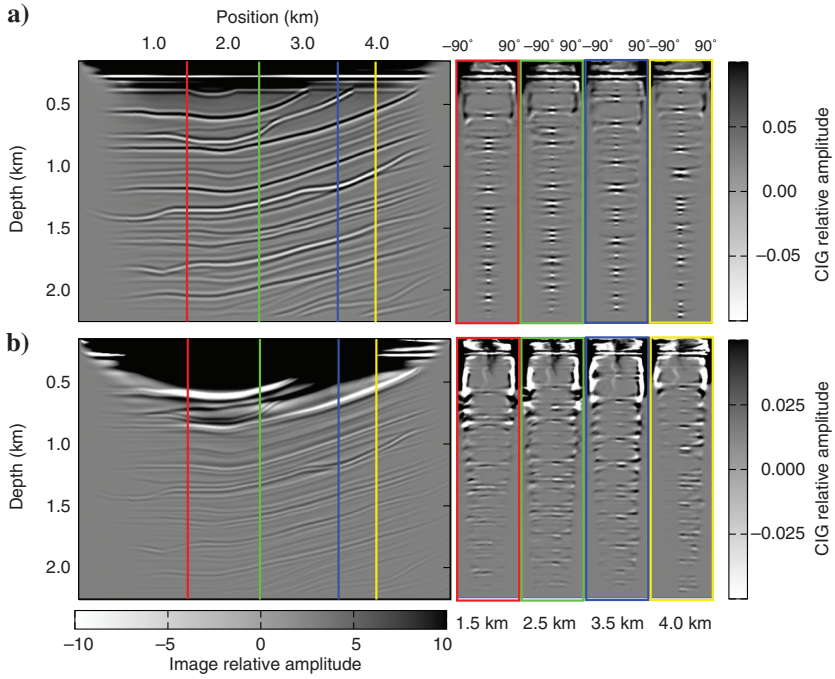

Figure 10. Elastic RTM images using crosscorrelation of corresponding components directly. (a and b) $\mathbf{I}_{zz}$ and $\mathbf{I}_{xx}$ stacked images (left) and their corresponding representative ADCIGs (right) at four horizontal locations.

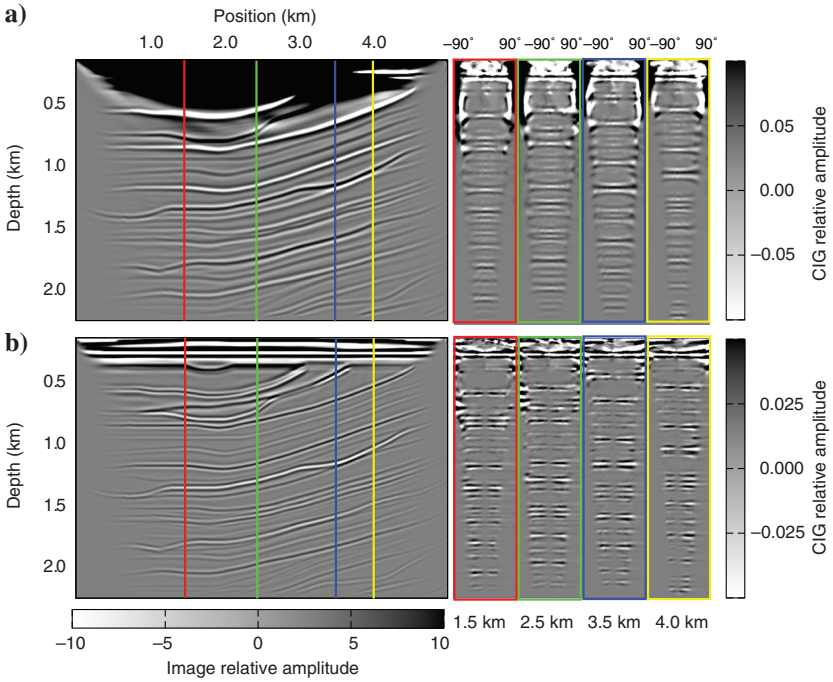

Figure 11. Elastic RTM images using only P/S decomposition. (a and b) $\mathbf{I}_{PP}$ and $\mathbf{I}_{PS}$ stacked images (left) and their corresponding representative ADCIGs (right) at four horizontal locations.

DISCUSSION

The up/down wavefield separation algorithm is based on complex wavefield extrapolation. Compared with traditional (real) wavefield extrapolation, the computational cost is doubled because a complex wavefield, instead of a real wavefield, is extrapolated. The up/down separation of an x-z snapshot can be performed at any time step, but two 1D Fourier transforms are needed at each x to perform the separation, which also increases the cost. However, it is still much cheaper than storing the wavefields at all time steps and performing 2D Fourier transforms.

Liu et al.'s (2011) method involves real, rather than complex, wavefield extrapolation, and so it is more efficient when applied to acoustic RTMs. Liu's imaging condition selectively crosscorrelates source and receiver wavefield pairs with opposite propagation directions along the z-axis, but the source and receiver wavefields are not up/down separated, and thus they are not available for observation and analysis by wavefield-based applications, such as Poynting vectors. Another disadvantage of Liu et al.'s (2011) method is that the up/down and down/up images

are not separable, whereas the algorithm in this paper can generate these two images separately for artifact analysis (for further discussion, see Wang et al., 2016). More importantly, Liu et al.'s (2011) imaging condition is built in the acoustic context and cannot be applied directly to the vector-based elastic RTM imaging condition, which requires a polarity calculation (Wang and McMechan, 2015). So the choice of algorithm depends on the context and on the desired output.

The ideas that form the basis of the up/down and P/S decomposition algorithms are straightforward and are easy to implement with minimum modifications to existing migration codes. A global Fourier transform in the vertical direction is sufficient for up/down separation of snapshot data from arbitrary velocity models because the separation does not depend on velocity (equations 5 and 6).

The elastic wavefield decomposition discussed in this paper is not perfect. A limitation exists during the up/down wavefield separation for VSP and snapshots when the values of vertical wavenumber k_z become very small (even zero), which means the waves are propagating horizontally, so a wavenumber truncation at $k_z = 0$ is introduced by the up/down separation algorithm (equations 5 and 6). This discontinuity generates artifacts in the inverse Fourier transform, so we apply a slight tapering of the low wavenumbers for positive and negative parts of the complex wavefield after the forward spatial Fourier transform to smooth the discontinuity, but the trade-off is losing that part of the signal. Overlapped wavefronts of the same wave mode are still inseparable if both have k_z components of the same sign. However, the algorithm is not limited to up/down separation; it is also applicable for separating wavefields in any direction by changing the direction of the spatial Fourier transforms (Tang and McMechan, 2016). This allows accurate separation of incident and reflected waves that are propagating more horizontally than vertically (such as turned reflections that image salt flanks), by doing the Fourier transform in the horizontal, rather than the vertical, direction. Directional binning (Tang and McMechan, 2016) can also be used to decompose the wavefield along different directions. Ideally, the up/down separation should be referenced to the local reflection normal direction, but this is expensive.

Another related limitation in the up/down separation is when aliased noise is present in the data, either in the depth direction (in which the Fourier transform is performed) or in time (in which the Hilbert transform is performed). When data are aliased, there is not a clear separation between the positive and negative apparent propagation directions (because of the spectral wraparound), so the up/down separation is also aliased.

A complication in applying the proposed separation algorithm to VSP field data occurs if the receivers are unevenly spaced in a borehole. Interpolation can be applied before the FFT over the z-axis if the data are not aliased. Another option is to use the original integral definition of the Fourier transform to handle uneven trace spacings rather than an FFT. Because wavefield extrapolations for field and synthetic data are performed on equally spaced model grids, one need only ensure that the input seismograms are correct to perform

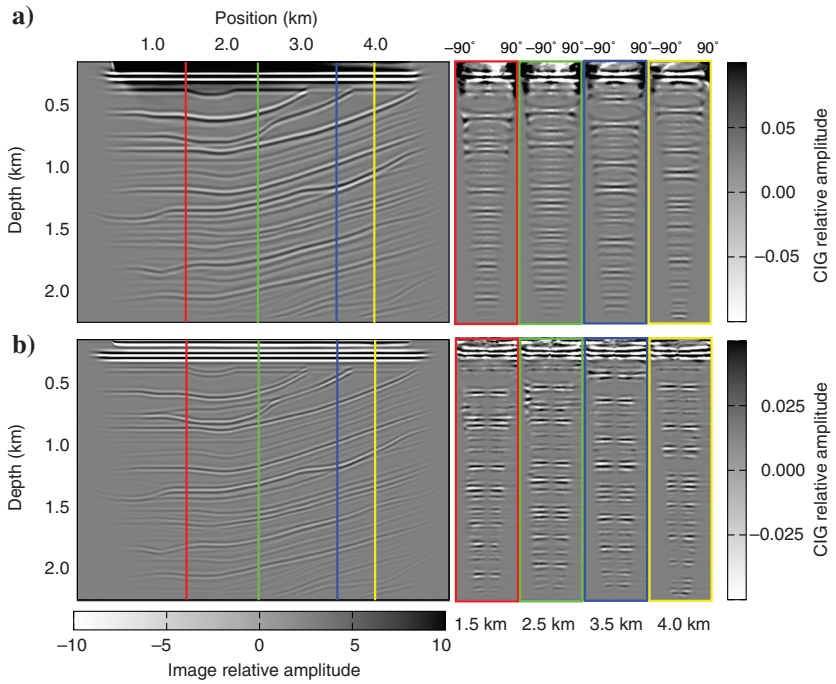

Figure 12. Elastic RTM images using P/S and up/down decompositions. (a and b) $\mathbf{I}_{PP}$ and $\mathbf{I}_{PS}$ stacked images (left) and their corresponding representative ADCIGs (right) at four horizontal locations.

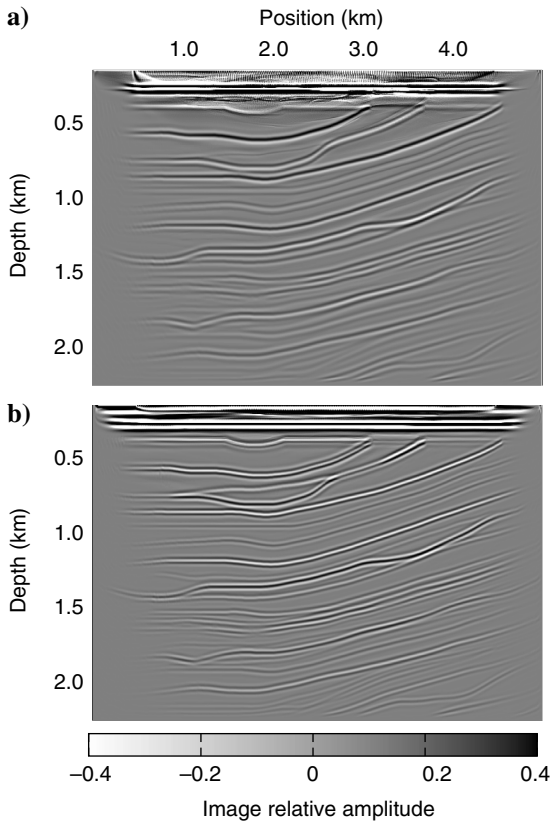

Figure 13. (a) PP and (b) PS images after Laplacian filtering of Figure 11a and 11b, respectively.

the up/down separation of the wavefield snapshots. If the VSP well is not vertical, it is still possible to separate the up-/down-going and P/S waves, provided that the data are not aliased in space along the well. As the positions of VSP receivers are known, we can still perform the leftward-rightward (or rightward-leftward) extrapolations to decompose the P- and S-waves. A modification of the approach discussed above is that the complex VSP traces can be generated first, used as boundary conditions for complex wavefield extrapolations, then up- and down-going waves can be separated in snapshots (rather than in recorded VSP data) before they are separately recorded again at the original VSP receiver positions. Inconsistency in different components of VSP data will lead to an incomplete P/S decomposition, as the relations between particle motions are distorted. This is not a problem for up/down separation because it is done separately for the individual components, but inconsistencies between the components in the input data will remain in the separated data.

In this paper, only the down-going source (P) wavefield cross-correlated with up-going receiver (P and S) wavefield (down/up) images are demonstrated, but a total number of 16 images can be generated for target-oriented analysis (Wang et al., 2016); e.g., the imaging of a salt-flank depends mainly on turning waves, which is better focused on the up/down images.

All the tests in this paper are based on nondispersive elastic equations. Application to dispersive (e.g., viscoelastic) equations is also possible because the real and imaginary parts the complex wavefield have the same amount of dispersion during extrapolation. Further investigations are in progress.

CONCLUSIONS

An up- and down-separation algorithm based on the properties of complex traces is illustrated and extended from acoustic to elastic wavefields, as well as combined with P- and S-waves decomposition by decoupled propagation to better analyze the wavefields. The up/down separation of a propagating wavefield is achieved by using complex wavefield extrapolation, which is much cheaper than separation methods via Fourier transforms over time because the latter requires saving the wavefield at all time steps. Tests using synthetic data show very good separation results on the elastic VSP data and on the propagating wavefield snapshots. Poynting vectors computed using the up/down separated wavefields are accurate for overlapped up- and down-going P- and S-waves. Elastic RTMs on synthetic data from the Marmousi2 model data show encouraging improvements when up/down and P/S decompositions are applied.

ACKNOWLEDGMENTS

The research leading to this paper is supported by the sponsors of the UT-Dallas Geophysical Consortium. A portion of the computations were done at the Texas Advanced Computing Center. This paper is contribution no. 1283 from the Department of Geosciences at UT-Dallas.

APPENDIX A

GENERATING DISCRETE-TIME ANALYTIC SIGNALS

Equation 7 is mathematically correct, but it does not include the details that are required to do a reliable numerical construction of an analytic signal. To construct the complex traces, we use the procedure of Maple (1999) for generating the discrete-time analytic signal, as follows:

1) Assume that a discrete wavelet or a seismic trace $\mathbf{d}$ at fixed x-position is an N-point time series, and N is an even number, which is preferable for FFTs. Applying a forward Fourier transform using the FFT $\mathcal{F}$ gives its N-point spectrum

$$\mathbf{X} = \mathcal{F}[\mathbf{d}]. \tag{A-1}$$

2) Form the N-point spectrum $[\mathbf{Y}]$ of the complex trace $[\tilde{\mathbf{d}}]$ with the procedure

$$Y(n) = \begin{cases} X(1), & \text{if } n = 1, \\ 2X(n), & \text{if } 2 \le n \le \frac{N}{2}, \\ X(n), & \text{if } n = \frac{N}{2} + 1, \\ 0, & \text{if } \frac{N}{2} + 2 \le n \le N. \end{cases} \tag{A-2}$$

Special treatments of the zero frequency ($n = 1$) and Nyquist frequency ($n = [N/2] + 1$) are necessary to give the correct cyclic behavior between the negative and positive frequency parts of the spectrum (Maple, 1999).

3) Perform the inverse Fourier transform to give the complex seismic trace

$$\tilde{\mathbf{d}} = \mathcal{F}^{-1}[\mathbf{Y}]. \tag{A-3}$$

Equation 7 is equivalent to equations A-1 to A-3 only when the zero and Nyquist frequencies on the spectrum have no significant values.

APPENDIX B

CALCULATIONS OF POYNTING VECTORS FROM DECOMPOSED P- AND S-WAVES

Poynting vectors of elastic wavefields are calculated using equation 9 with particle velocity and stresses (Červený, 2001; Dickens and Winbow, 2011). In the (2D) matrix form

$$\begin{bmatrix} s_x \\ s_z \end{bmatrix} = -\begin{bmatrix} \tau_{xx} & \tau_{xz} \\ \tau_{xz} & \tau_{zz} \end{bmatrix} \begin{bmatrix} v_x \\ v_z \end{bmatrix}, \tag{B-1}$$

which is for the P/S coupled wavefield. To calculate the Poynting vectors of P- and S-waves separately, the corresponding P- and S-wave stress tensors and particle velocities are needed.

The elastodynamic equations (Virieux, 1986; Levander, 1988) are composed of the equation of motion

$$\rho \frac{\partial^2 u_x}{\partial t^2} = \frac{\partial \tau_{xx}}{\partial x} + \frac{\partial \tau_{xz}}{\partial z}, \tag{B-2}$$

$$\rho \frac{\partial^2 u_z}{\partial t^2} = \frac{\partial \tau_{zz}}{\partial z} + \frac{\partial \tau_{xz}}{\partial x}, \tag{B-3}$$

and the general Hooke's law

$$\tau_{xx} = M_P \left(\frac{\partial u_x}{\partial x} + \frac{\partial u_z}{\partial z} \right) - 2M_S \frac{\partial u_z}{\partial z}, \tag{B-4}$$

$$\tau_{zz} = M_P\left(\frac{\partial u_z}{\partial z} + \frac{\partial u_x}{\partial x}\right) - 2M_S\frac{\partial u_x}{\partial x}, \tag{B-5}$$

$$\tau_{xz} = M_S\left(\frac{\partial u_z}{\partial x} + \frac{\partial u_x}{\partial z}\right), \tag{B-6}$$

or in a matrix form

$$\boldsymbol{\tau} = \begin{bmatrix} \tau_{xx} & \tau_{xz} \\ \tau_{xz} & \tau_{zz} \end{bmatrix} = \begin{bmatrix} M_P\left(\frac{\partial u_x}{\partial x} + \frac{\partial u_z}{\partial z}\right) - 2M_S\frac{\partial u_z}{\partial z} & M_S\left(\frac{\partial u_z}{\partial x} + \frac{\partial u_x}{\partial z}\right) \\ M_S\left(\frac{\partial u_z}{\partial x} + \frac{\partial u_x}{\partial z}\right) & M_P\left(\frac{\partial u_z}{\partial z} + \frac{\partial u_x}{\partial x}\right) - 2M_S\frac{\partial u_x}{\partial x} \end{bmatrix}, \tag{B-7}$$

where u_x and u_z are the horizontal and vertical particle displacements, and the particle velocities v_x and v_z can be calculated by taking time derivatives of u_x and u_z; M_P is the P-wave modulus and M_S is the S-wave modulus. To obtain the pure P- or S-wave mode equations, one can simply make $M_S = 0$ (to get the P-wave) or $M_P = 0$ (to get the S-wave) in equations B-4 to B-6. Then, we obtain the P-wave stress tensor

$$\boldsymbol{\tau}^P = \begin{bmatrix} M_P\left(\frac{\partial u_x}{\partial x} + \frac{\partial u_z}{\partial z}\right) & 0 \\ 0 & M_P\left(\frac{\partial u_x}{\partial x} + \frac{\partial u_z}{\partial z}\right) \end{bmatrix}. \tag{B-8}$$

The P-wave Poynting vector can be formed as a product of P-wave stress tensor and P-wave particle velocities

$$\begin{bmatrix} s_x^P \\ s_z^P \end{bmatrix} = -\begin{bmatrix} M_P\left(\frac{\partial u_x}{\partial x} + \frac{\partial u_z}{\partial z}\right) & 0 \\ 0 & M_P\left(\frac{\partial u_x}{\partial x} + \frac{\partial u_z}{\partial z}\right) \end{bmatrix}\begin{bmatrix} v_x^P \\ v_z^P \end{bmatrix}. \tag{B-9}$$

Because the off-diagonal terms of the P-wave stress tensor B-8 are zeros and diagonal terms are equal, thus, the P-wave stress tensor can be expressed as a scalar $\tau^P = M_P[(\partial u_x/\partial x) + (\partial u_z/\partial z)]$; thus, equations B-9 and 10 are equivalent.

Similarly, the S-wave stress tensor has the form

$$\boldsymbol{\tau}^S = \begin{bmatrix} -2M_S\frac{\partial u_z}{\partial z} & M_S\left(\frac{\partial u_z}{\partial x} + \frac{\partial u_x}{\partial z}\right) \\ M_S\left(\frac{\partial u_z}{\partial x} + \frac{\partial u_x}{\partial z}\right) & -2M_S\frac{\partial u_x}{\partial x} \end{bmatrix}, \tag{B-10}$$

and the S-wave Poynting vector

$$\begin{bmatrix} s_x^S \\ s_z^S \end{bmatrix} = -\begin{bmatrix} -2M_S\frac{\partial u_z}{\partial z} & M_S\left(\frac{\partial u_z}{\partial x} + \frac{\partial u_x}{\partial z}\right) \\ M_S\left(\frac{\partial u_z}{\partial x} + \frac{\partial u_x}{\partial z}\right) & -2M_S\frac{\partial u_x}{\partial x} \end{bmatrix}\begin{bmatrix} v_x^S \\ v_z^S \end{bmatrix}. \tag{B-11}$$

Notice the stress tensors have the relation (compared with equation B-7)

$$\boldsymbol{\tau} = \tau^P + \boldsymbol{\tau}^S, \tag{B-12}$$

thus, equations B-11 and 11 are equivalent.

REFERENCES

Červený, V., 2001, Seismic ray theory: Cambridge University Press.

Chen, K., 2014, Finite-difference simulation of elastic wave with separation in pure P- and S-modes: Journal of Computational Methods in Physics, **2014**, 1–14, doi: 10.1155/2014/108713.

Chen, T., and B. He, 2014, A normalized wavefield separation cross-correlation imaging condition for reverse time migration based on Poynting vector: Applied Geophysics, **11**, 158–166, doi: 10.1007/s11770-014-0441-5.

Dash, R., G. Spence, R. Hyndman, S. Grion, Y. Wang, and S. Ronen, 2009, Wide-area imaging from OBS multiples: Geophysics, **74**, no. 6, Q41–Q47, doi: 10.1190/1.3223623.

Dickens, T. A., and G. A. Winbow, 2011, RTM angle gathers using Poynting vectors: 81st Annual International Meeting, SEG, Expanded Abstracts, 3109–3113.

Fei, T. W., Y. Luo, and F. Qin, 2014, An endemic problem in reverse-time migration: 84th Annual International Meeting, SEG, Expanded Abstracts, 3811–3815.

Gabor, D., 1946, Theory of communications: Journal of the Institution of Electrical Engineers, **93**, 429–457.

Havlicek, J. P., J. W. Havlicek, N. D. Mamuya, and A. C. Bovik, 1998, Skewed 2D Hilbert transforms and computed AM-FM models: Proceedings of the IEEE International Conference on Image Processing, 602–606, doi: 10.1109/ICIP.1998.723573.

Hu, L., and G. A. McMechan, 1987, Wave-field transformations of vertical seismic profiles: Geophysics, **52**, 307–321, doi: 10.1190/1.1442305.

Jin, H., G. A. McMechan, and H. Guan, 2014, Comparison of methods for extracting ADCIGs from RTM: Geophysics, **79**, no. 3, S89–S103, doi: 10.1190/geo2013-0336.1.

Komatitsch, D., and R. Martin, 2007, An unsplit convolutional perfectly matched layer improved at grazing incidence for the seismic wave equation: Geophysics, **72**, no. 5, SM155–SM167, doi: 10.1190/1.2757586.

Levander, A. R., 1988, Fourth-order finite-difference P-SV seismograms: Geophysics, **53**, 1425–1436, doi: 10.1190/1.1442422.

Liu, F., G. Zhang, S. A. Morton, and J. P. Leveille, 2011, An effective imaging condition for reverse-time migration using wavefield decomposition: Geophysics, **76**, no. 1, S29–S39, doi: 10.1190/1.3533914.

Ma, D., and G. Zhu, 2003, P- and S-wave separated elastic wave equation numerical modeling (in Chinese): Oil Geophysical Prospecting, **38**, 482–486.

Maple, S. L., Jr., 1999, Computing the discrete-time "analytic" signal via FFT: IEEE Transactions on Signal Processing, **47**, 2600–2603, doi: 10.1109/78.782222.

Martin, G. S., K. J. Marfurt, and S. Larsen, 2002, Marmousi-2: An updated model for the investigation of AVO in structurally complex areas: 72nd Annual International Meeting, SEG, Expanded Abstracts, 1979–1982.

Sun, R., 1999, Separating P- and S-waves in a prestack 2-dimensional elastic seismogram: 61st Annual International Conference and Exhibition, EAGE, Extended Abstracts, paper 6–23, doi: 10.3997/2214-4609.201407744.

Sun, R., and G. A. McMechan, 2001, Scalar reverse-time depth migration of prestack elastic seismic data: Geophysics, **66**, 1519–1527, doi: 10.1190/1.1487098.

Tang, C., and G. A. McMechan, 2016, Multidirection slowness vector for computing angle gathers from reverse-time migration: Geophysics, **81**, no. 2, S11–S24, doi: 10.1190/geo2015-0134.1.

Tang, B., S. Xu, and Y. Zhang, 2013a, 3D angle gathers with plane-wave reverse-time migration: Geophysics, **78**, no. 3, S117–S123, doi: 10.1190/geo2012-0313.1.

Tang, C., D. Wang, and J. Hao, 2013b, RTM angle gathers with Gaussian weighted time-lapse Poynting vectors and receiver wavefield reconstruction in forward time direction: 83rd Annual International Meeting, SEG, Expanded Abstracts, 3779–3783.

Ville, J. A., 1948, Theorie et application de la notion du signal analytique: Cables Transmission, **2**, 61–74.

Virieux, J., 1986, P-SV wave propagation in heterogeneous media: Velocity-stress finite-difference method: Geophysics, **51**, 889–901, doi: 10.1190/1.1442147.

Wang, F., H. Chauris, D. Donno, and H. Calandra, 2013, Taking advantage of wavefield decomposition in full waveform inversion: 75th Annual International Conference and Exhibition, EAGE, Extended Abstracts, paper Tu0708.

Wang, W., and G. A. McMechan, 2015, Vector-based elastic reverse-time migration: Geophysics, **80**, no. 6, S245–S258, doi: 10.1190/geo2014-0620.1.

Wang, W., G. A. McMechan, and F. Xie, 2016, Analysis of up/down decomposed acoustic RTM images: Geophysics, **81**, this issue, doi: 10.1190/geo2015-0612.1.
Wang, W., G. A. McMechan, and Q. Zhang, 2015, Comparison of two algorithms for isotropic elastic P and S decomposition in the vector domain: Geophysics, **80**, no. 4, T147–T160, doi: 10.1190/geo2014-0563.1.
Weglein, A. B., 1999, Multiple attenuation: An overview of recent advances and the road ahead: The Leading Edge, **18**, 40–44, doi: 10.1190/1.1438150.
Wenschel, P. C., 1976, The vertical array in reflection seismology — Some experimental studies: Geophysics, **41**, 219–232, doi: 10.1190/1.1440612.
White, J. E., 1965, Seismic waves: Radiation, transmission and attenuation: McGraw-Hill Book Company.
Xiao, X., and W. S. Leaney, 2010, Local vertical seismic profiling (VSP) elastic reverse-time migration and migration resolution: Salt-flank imaging with transmitted P-to-S waves: Geophysics, **75**, no. 2, S35–S49, doi: 10.1190/1.3309460.
Xie, X., and R. Wu, 2002, Extracting angle domain information from migrated wavefield: 72nd Annual International Meeting, SEG, Expanded Abstracts, 1360–1363.
Yan, J., and W. Ross, 2013, Improving the stability of angle gather computation using Poynting vectors: 83rd Annual International Meeting, SEG, Expanded Abstracts, 3784–3788.
Yan, J., and P. Sava, 2008a, Elastic wavefield separation for VTI media: 78th Annual International Meeting, SEG, Expanded Abstracts, 2191–2195.
Yan, J., and P. Sava, 2008b, Isotropic angle-domain elastic reverse-time migration: Geophysics, **73**, no. 6, S229–S239, doi: 10.1190/1.2981241.
Zhang, Q., 2014, RTM angle gathers and specular filter (SF) RTM using optical flow: 84th Annual International Meeting, SEG, Expanded Abstracts, 3816–3820.
Zhang, Q., and G. A. McMechan, 2010, 2D and 3D elastic wavefield vector decomposition in the wavenumber domain for VTI media: Geophysics, **75**, no. 3, D13–D26, doi: 10.1190/1.3431045.
Zhang, Q., and G. A. McMechan, 2011, Direct vector-field method to obtain angle-domain common-image gathers from isotropic acoustic and elastic reverse time migration: Geophysics, **76**, no. 5, WB135–WB149, doi: 10.1190/geo2010-0314.1.
Zhang, Y., and J. Sun, 2009, Practical issues in reverse time migration: True amplitude gathers, noise removal and harmonic source encoding: First Break, **26**, 29–35.
Zhang, J., Z. Tian, and C. Wang, 2007a, P- and S-wave separated elastic wave equation numerical modeling using 2D staggered-grid: 77th Annual International Meeting, SEG, Expanded Abstracts, 2104–2109.
Zhang, Y., G. Zhang, D. Yingst, and J. Sun, 2007b, Explicit marching method for reverse-time migration: 77th Annual International Meeting, SEG, Expanded Abstracts, 2300–2304.